Innovative Characterization of Amorphous and Thin-Film Silicon for Improved Module Performance

Annual Subcontract Report: 28 April 2006 – 27 April 2007

J. David Cohen
Department of Physics and Materials Science Institute
University of Oregon, Eugene, Oregon

Prepared for the National Renewable Energy Laboratory

under Subcontract No. ZXL-5-44205-11

NREL Technical Monitor: B. von Roedern

PREFACE

This Annual Technical Progress Report covers the work performed at the University of Oregon for the period 28 April 2005 - 27 April 2006 under NREL Subcontract Number ZXL-5-44205-11. The following personnel participated in this research program:

NAME	TITLE	WORK PERFORMED
J. David Cohen	Principal Investigator	Program Manager
Shouvik Datta	Research Associate	Properties of NREL HWCVD a-Si,Ge:H alloys
Peter Hugger	Research Assistant	Properties of United Solar nc-Si:H materials
Pete Erslev (Half Time)	Research Assistant	Studies of Cu(InGa)Se$_2$ photovoltaic devices.

TABLE OF CONTENTS

LIST OF ILLUSTRATIONS

LIST OF TABLES

EXECUTIVE SUMMARY

Our work under NREL Subcontract ZXL-5-44205-11 during Phase II has focused on three areas of study. First, we used transient photocapacitance (TPC) spectroscopy, transient photocurrent (TPI) and drive-level capacitance profiling (DLCP) to characterize the electronic properties of hydrogenated nanocrystalline Si (nc-Si:H) within an extensive new set of working n-i-p sample devices produced at United Solar Ovonics Corporation. These were all deposited on specular stainless-steel under four different types of hydrogen profiling, and each deposition contained samples with varying degrees of crystalline fractions. Our data suggests that the degree of crystallinity in these nc-Si:H samples, rather than the hydrogen profiling function itself, was the strongest factor determining the defect response in our junction capacitance measurements. We also found that the samples that contained a higher fraction of amorphous component, as determined from Raman spectroscopy, exhibited the highest *resilience* to light-induced deep defect creation, while the samples with estimated crystalline fractions above 60vol.% exhibited quite a pronounced increase of deep defects after light soaking.

Second, we continued our studies of the lower filament temperature HWCVD a-Si,Ge:H alloys being developed at NREL. This year we focused on a set of samples in which controlled levels of oxygen impurities were introduced, ranging from below 10^{19}cm^{-3} to roughly 5×10^{20}cm^{-3}. We discovered that the oxygen was responsible for a distinct deep defect, with an optical transition lying roughly 1.3 to 1.4 eV above the valence band, and we hypothesize that the this impurity related defect state may be associated with a positively charged oxygen donor level. Moreover, because the electrons excited into this defect remain trapped for roughly 0.5s at temperatures up to 370K, this strongly implies that there must exist a large barrier to their subsequent thermal emission into the conduction band.

Third, we used our junction capacitance methods to study the effect of Na on CIGS thin film solar cells. Our DLCP measurements revealed an increased free carrier density with when Na was present, and also indicated a higher density of bulk defects in CIGS absorber. The sub-band-gap TPC spectra showed a broader defect band and a steeper Urbach energy with the addition of Na which implies an increase in the carrier mobilities. However, none of these changes were large enough to account for the >40% increase in efficiency with the addition of Na. Ultimately, forward bias admittance measurements revealed the existence of a large defect density at the CdS/CIGS heterojunction for the low Na sample. We argue that such a defect could readily explain the loss in V_{OC} in the sample with reduced Na, and would be consistent with the observed admittance and DLCP behavior for this sample. Thus, it appears that it is the passivation of these interfacial defects that primarily accounts for the beneficial effects of Na toward the increased performance of the CIGS solar cells fabricated at IEC.

1.0 INTRODUCTION

The work carried out during Phase II under NREL Subcontract ZXL-5-44205-11 has focused primarily on three subject areas. First, we have been continuing to evaluate the nanocrystalline Si material under development at United Solar Ovonics Corporation (USOC) which will be denoted in this report as nc-Si:H. It is hoped that such materials may ultimately be able to replace one of a-Si,Ge:H layers in an amorphous silicon triple junction device. This year's work has focused on evaluating an extensive new series of United Solar sample devices, deposited on specular stainless substrates using four types of hydrogen profiling functions and, by virtue of a spatially varying glow discharge intensity across the substrate, different crystalline fractions. All of the samples studied were finished n-i-p devices. Of particular interest were the observed differences in the deduced light induced deep defect creation behavior for these samples depending on their crystalline fractions.

Our second major focus has been in the continuing evaluation of amorphous silicon-germanium alloys produced by the hot-wire CVD growth process by Yueqin Xu at NREL. In particular we have been examining in more detail the effects of oxygen at varying levels introduced intentionally using a controlled air leak-valve. This has led to the discovery of optical transition at a energy near 1.3eV between the valence band and an empty oxygen related defect level in the mobility gap. Through a study of temperature dependence of this feature we have concluded that there must exist a large barrier to the subsequent thermal emission of the electron into the conduction band. We hypothesize that the observed oxygen impurity related defect state may be associated with a positively charged oxygen donor level, possibly the previously suggested three fold coordinated oxygen center (O_3^+).

Finally, we continued studies to characterize the electronic properties of copper indium-gallium diselenide (CIGS) materials. Our CIGS related studies are supposed to account for roughly 30% of our work under our Thin-Film Partnership Subcontract. The goal of this work is to try to identify the reasons for the vastly different performance levels of laboratory based devices compared to CIGS devices produced by growth processes more suitable to large scale manufacturing. This year we carried out studies designed to identify the beneficial effects of Na impurities on CIGS photovoltaic devices. Our approach, in collaboration with Bill Shafarman's group at IEC, University of Delaware, was to compare in detail the electronic properties of two CIGS sample devices that were co-deposited onto two different substrates: one with the usual soda-lime glass, and one employing a SiO_2 blocking layer to mostly prevent the diffusion of Na into the CIGS absorber. Although the efficiencies of the higher-Na device was more than 40% higher, we found that most differences in the electronic properties of the CIGS absorbers themselves were not significant enough to account for this.

2.0 SAMPLES

2.1 UNITED SOLAR NANOCRYSTALLINE SILICON

In addition to two sets of nc-Si:H sample devices obtained from United Solar (B. Yan) during the previous Subcontract year, an extensive additional set was received early in 2007. These were produced from 4 separate depositions with different types of hydrogen concentration variations in each deposition; specifically, constant in time, square root in time, linear in time, and quadratic in time. Each substrate was processed to yield more than 30 devices, and the properties of these were different because the plasma varied over the diameter of the substrate. This meant that the devices near the center of the substrate were more crystalline, while those near the edge were more amorphous. Table I lists the sample devices we received for study and their performance parameters. In each deposition "Cell 74" was close to the center and thus had the highest crystalline fraction, "Cell 94" had the highest amorphous fraction, and "Cell 75" was an intermediate case. This is also indicated in the schematic of the cell positions shown in Fig. 1.

We employed Raman spectroscopy at 785nm to quantify the crystalline and amorphous fractions for this set of samples. An example for the 15125 (constant H dilution) sample set is shown in Fig. 2. Here we compare the Raman spectra for the most crystalline (74) and most amorphous (94) sample device. Each of these spectra has been analyzed by separation into 2 Gaussian components centered at 480 cm^{-1} and 510 cm^{-1}, and one Gaussian/Lorentzian mixed component at 520 cm^{-1}, as indicated by the green curves in Fig. 2. Based upon such analyses of the Raman spectra we have estimated the crystalline fraction for each of the samples listed in Table I. These are tabulated in Table II.

Table I. Set of USOC nc-Si:H samples to investigate detailed effects of hydrogen profiling methods on devices with different degrees of crystallinity.

Run	Profiling	Cell	Pmax	Jsc	Voc	ff
15125	constant	94	3.51	11.86	0.597	0.496
15125	constant	75	4.31	15.57	0.53	0.522
15125	constant	74	3.95	14.89	0.501	0.529
15123	t^1/2	94	4.77	15.67	0.609	0.499
15123	t^1/2	75	4.94	16.12	0.534	0.575
15123	t^1/2	74	4.99	16.62	0.51	0.589
15117	linear	94	4.38	14.46	0.747	0.406
15117	linear	75	4.95	16	0.54	0.572
15117	linear	74	4.96	16.53	0.509	0.59
15121	t^2	94	3.96	11.57	0.859	0.399
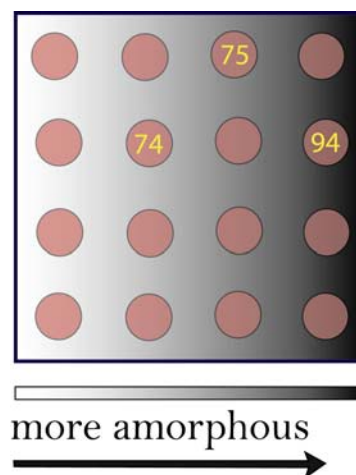
FIG. 1. Layout of USOC nc-Si:H devices on substrate indicating the variation of the amorphous/ crystallinity fractions with position.

FIG. 2. Raman spectra obtained at 785nm for two nc-Si:H devices from the same deposition but at different positions on the substrate. The top spectrum was taken for a device near the middle of the substrate, and it contains a much higher crystalline fraction, than that of a device near the edge of the substrate, shown at the bottom. The thin green lines indicate a decomposition of each of these spectra into 3 components to enable an estimate of the crystalline fractions to be made. These estimates are listed in Table II.
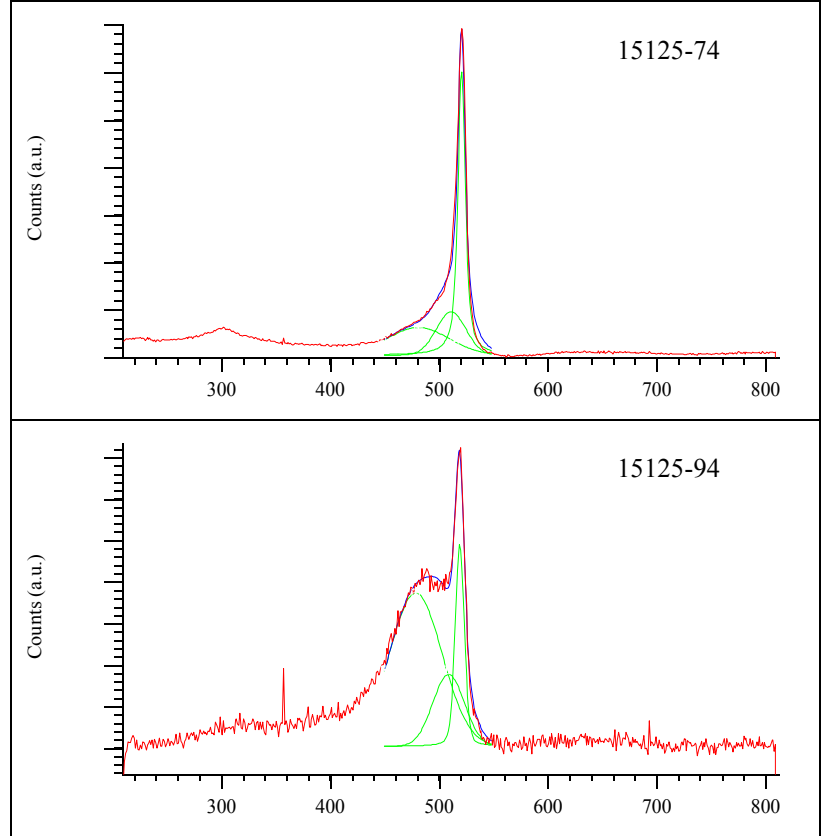
Table II. Summary of Raman spectral analysis for United Solar nc-Si:H samples. These spectra have been separated into 3 components centered at 480, 510, and 520 cm^{-1} as illustrated in Fig. 2. This allows the crystallite fractions to be estimated [1,2].

Run	Cell	Profiling	I(~480cm^{-1})	I(~510 cm^{-1})	I(~520 cm^{-1})	Xc
15125	94	constant	229594	64661	58374	0.36
15125	75	constant	831052	327430	826590	0.59
15125	74	constant	417259	315852	707088	0.72
15123	94	t^1/2	2.24E+06	271741	303997	0.21
15123	75	t^1/2	1.04E+06	355527	1.41E+06	0.64
15123	74	t^1/2	329199	157610	537355	0.69
15117	94	linear	3.09E+06	867597	1.55E+06	0.45
15117	75	linear	3.14E+06	1.54E+06	2.59E+06	0.58
15117	74	linear	2.66E+06	896825	2.51E+06	0.67
15121	94	t^2	894569	389640	805516	0.59
15121	75	t^2	348128	69828	268511	0.51
15121	74	t^2	91146	49666	146672	0.69

Table III. Full set of HWCVD a-Si,Ge:H samples obtained from NREL in early 2006 to examine effects of intentional oxygen contamination.

Samples' ID	Ts_starting °C	Ts_ending °C	Deposition Time(min)	SiH4	Used Gases: GeH4*	H2	air-leaking sccm
L1628	204	289	150	26.4	6.3	30	no
L1629	204	284	130	26.4	6.3	30	0.06
L1630	204	289	140	26.4	6.3	30	0.02
L1631	204	275	130	26.4	6.3	30	0.2

All above are a-SiGe:H alloys with Ge_% about ~29-32%

L1632	204	315	150	30		0	no
L1633	204	295	165	26.4		26.4	no
L1634	205	315	150	30		0	0.06

All above are a-Si:H films with no Ge

L1636	205	289	200	26.6	2.7	28	no
L1637	205	292	180	26.6	2.7	28	0.02
L1640	205	292	180	26.6	2.7	28	0.06
L1641	205	288	150	26.6	2.7	28	0.2

All above are a-SiGe:H alloys with Ge_% about ~15%

2.2 NREL HOT-WIRE CVD AMORPHOUS SILICON-GERMANIUM ALLOYS

For the last couple years we have been examining the electronic properties of HWCVD a-Si,Ge:H alloys deposited at NREL using a lower filament temperature process. For a long time the hot-wire CVD method was generally unsuccessful for the a-Si,Ge:H alloys, resulting in materials with anomalously large deep defect densities and broad band tails.[3] However, by employing tantalum filaments held at somewhat lower temperature (1800°C), we found that the electronic properties for these a-Si,Ge:H alloys were quite good.

However, a series of films deposited in 2005 appeared to have considerably poorer electronic properties and it seemed plausible that the problem might be due to higher oxygen levels. Thus, we decided to specifically investigate the effects of oxygen contamination on these HWCVD deposited a-Si,Ge:H films in more detail after the source of the contamination was finally discovered and eliminated in the Fall, 2005. In early 2006 an extensive series of a-Si,Ge:H alloy samples were deposited using a controlled leak valve to introduce a systematic variation in oxygen level during the HWCVD process. Sets of samples with roughly 30at.% Ge, 15at.% Ge, and no Ge were prepared by Yueqin Xu. Films were deposited both on specular stainless steel (SS) substrates again coated with thin layers n$^+$ PECVD a-Si:H and simultaneously on heavily doped p$^+$ crystalline Si substrates. Typically a 1:1 hydrogen dilution
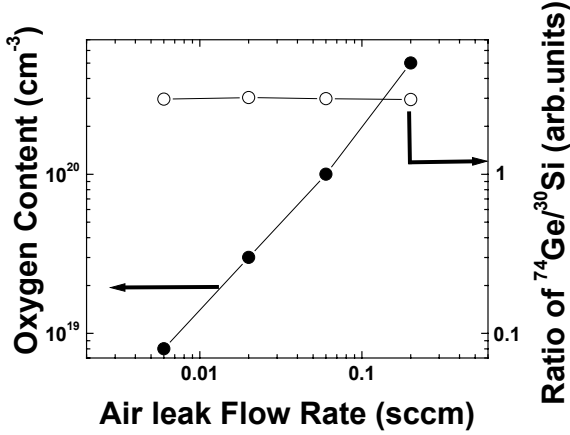
FIG. 3. Oxygen content for one series of the NREL HWCVD a-Si,Ge:H films and their relative fractions of Ge with respect to Si as measured by SIMS. Note the systematic increase in the oxygen level in the fillm with increase air leak flow rate as well as the nearly constant fraction of Ge (roughly 30at.%) in this series of samples. Data corresponding to 'no intentional air leak' was plotted against an imaginary flow rate of 0.006 sccm.

level [i.e., $H_2/(SiH_4 + GeH_4) = 1$] was maintained during the depositions. Growth rates typically varied between 1.5 to 2Å/s. The substrate temperatures were always set to 204°C at the beginning of film growth, but the final temperatures were higher (~280°C) due to filament heating. A semi-transparent Pd contact was again deposited on the top surface all samples to provide a top Schottky barrier for our junction-capacitance based measurements. However, in case of the samples deposited onto p^+ crystalline Si, we utilized the substrate barrier junction for our measurements. Detailed growth parameters for these HWCVD a-Si,Ge:H films are listed in Table III. SIMS measurements were carried out and indeed revealed a systematic increase of oxygen contamination as the air leak was gradually increased to 0.2sccm. Figure 3 shows the relative content of oxygen in the samples and germanium fraction with respect to Si for the nominally 30at.% Ge alloy series. At the same time, these SIMS measurements indicated that the N content ($<4 \times 10^{16}$ cm^{-3}) remained nearly constant.

2.3 THE ROLE OF SODIUM ON CIGS SOLAR CELLS

The addition of Na to Cu(InGa)Se$_2$ based solar cell devices is a commonly followed procedure, boosting the efficiency by up to 50% primarily through a sizeable increase in the open-circuit voltage (V_{oc}) and the fill factor (FF). Although the positive role of Na is well known in the fabrication of CIGS devices, there is an ongoing debate as to the exact mechanism of the beneficial effect of Na, with much of the debate centering around where in the cell the Na has its effect. Possible sites are grain boundaries, in the bulk of the grains, or the CdS/CIGS heterojunction. Recent experimental results appear quite contradictory, with one group finding no evidence of Na at the grain boundaries[4] and another group concluding that the Na is only found in significant amounts at the grain boundaries[5]. Another group hypothesized that the Na acts only during the growth of the sample to organize and passivate point defects[6]; however,

Table IV: Device performance parameters of the matched Cu(InGa)Se$_2$ devices simultaneously deposited on Mo coated soda lime glass (normal Na) and SiO$_2$ coated glass (reduced Na).

Cell	Voc (V)	Jsc (mA)	FF (%)	Eff (%)
34017.12 – 1 (Na)	0.624	32.9	74.0	15.2
34017.32 – 4 (reduced Na)	0.494	33.6	64.3	10.7

this is disputed by similar benefits obtained through diffusion of Na into the sample in a post-deposition treatment[7].

A pair of matched baseline (34017.12) and reduced Na (34017.32) samples were provided to us by the Institute of Energy Conversion in May, 2006. The samples were co-deposited at 550°C in a single deposition with a thickness of 2.0 μm. The baseline film was deposited on a Mo-coated soda lime glass substrate and the reduced Na film was deposited on a substrate provided by Shell Solar which has a SiO$_2$ diffusion barrier below the Mo. Both devices were completed with standard CdS, ZnO and ITO depositions and a Ni/Al grid. Table IV provides the device performance parameters of the cells analyzed and discussed below. These parameters were typical for all of the cells on the samples. The differences between these samples exhibit the commonly known effects of Na on CIGS solar cells: An increased V$_{oc}$, fill factor, and efficiency (by nearly 50%), with virtually no effect on short circuit current.

Secondary Ion Mass Spectroscopy (SIMS) was performed on a similar pair of samples. These profiles, shown in Fig. 4, indicate a difference in the relative Na density from a factor of five near the back contact to a factor of nearly 100 near the front between the Na and reduced Na samples. Thus, the Na appears to be segregating towards the front of the sample when it is intentionally added.
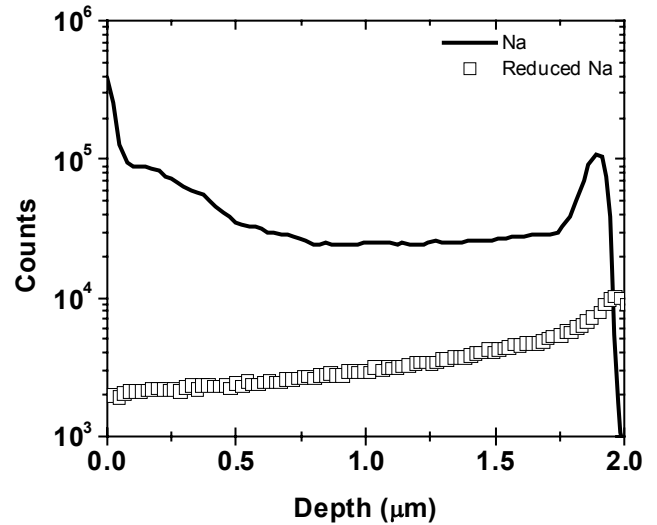

FIG. 4. SIMS depth profiles of a matched pair of higher and lower sodium Cu(InGa)Se$_2$ sample devices.

3.0 EXPERIMENTAL CHARACTERIZATION METHODS

The measurements employed in our studies rely on a set of experimental techniques which have all been described previously in some detail. They consist of (1) admittance

spectroscopy as a function of temperature and frequency, (2) drive-level capacitance profiling, and (3) transient photocapacitance taken together with transient junction photocurrent spectroscopy. Here we will summarize each method only very briefly.

3.1 ADMITTANCE SPECTROSCOPY

All of the sample devices studied contain a depletion region whose complex admittance is characterized as a function of temperature and frequency [see, for example, Fig. 1] before we undertake the more sophisticated capacitance based measurements described in Sections 3.2 and 3.3 below. Such measurements provide us with an estimate of our film thickness (the temperature independent region at low T is simply related to the geometric thickness, d, by the formula $C = \varepsilon A/d$), and an Arrhenius plot of the frequency of the lowest temperature capacitance step (or conductance peak) *vs*. 1/T provides us with the activation energy of the ac conductivity, E_{σ}, which we sometimes identify with the Fermi energy position: $E_{\sigma} = E_C - E_F$.[8] These admittance measurements also give us an indication of the quality of our barrier junction which allow us to pre-screen our samples for further study.

3.2 DRIVE-LEVEL CAPACITANCE PROFILING

The drive-level capacitance profiling method has been described in detail in many publications [9,10,11,12]. It is similar to other kinds of capacitance profiling in that it provides us with a density *vs*. distance profile; however, this particular method was developed specifically to address the difficulties encountered in interpreting capacitance measurements in materials with defect densities comparable to carrier densities. In this method we determine the junction capacitance both as a function of DC bias, V_B, and as a function of the amplitude of the alternating exciting voltage, δV: $C(V_B, \delta V) = C_0(V_B) + C_1(V_B)\,\delta V + ...$

An expression involving the coefficients C_0 and C_1 can then be used to deduce the free carrier density, n, plus an integral over the density of mobility gap defect states; specifically:

$$N_{DL} \equiv \frac{C_0^3}{2q_e \varepsilon A^2 C_1} \qquad = n + \int_{E_C-E_e}^{E_F^o} g(E)dE \quad \text{(n-type)} \quad \text{or} \quad = p + \int_{E_F^o}^{E_V+E_e} g(E)dE \quad \text{(p-type)} \qquad (1)$$

Here E_F^0 is the bulk Fermi level position in the sample and E_e depends on the frequency and temperature of measurement:

$$E_e(\omega, T) = k_B T \log(\nu/\omega) \qquad (2)$$

Thus, by altering the measurement temperature (or frequency) we obtain information about the energy distribution of the defects and, by altering the applied DC bias, we can vary the spatial

region at which we detect the defects in the sample. That is, we can spatially profile the defects as a function of the position from the barrier interface.

3.3 TRANSIENT PHOTOCAPACITANCE AND PHOTOCURRENT

The methods of junction transient photocapacitance and photocurrent have been discussed by us in great detail over the years in the literature [13,14,15] and also in many previous NREL reports. They represent types of sub-band-gap optical spectroscopy and provide spectra quite similar in appearance to PDS derived sub-band-gap optical absorption spectra or to CPM spectra. Instead of detecting absorbed energy, however, our photocapacitance and photocurrent transient methods detect the optically induced change in defect charge within the depletion region.

In this method the space charge region of the semiconductor near the barrier junction is first subjected to a voltage "filling pulse". This pulse causes a non-equilibrium (filled) occupation of gap states to be established. As time progresses, the initial steady-state population is recovered through the excitation of trapped electrons to the conduction band where they can then move out of the depletion region under the influence of the electric field. In the dark this process proceeds entirely by the thermal excitation of trapped carriers. However, this process can be enhanced through optical excitation and this is the basis of the photocapacitance and junction photocurrent techniques.

The re-equilibration can be observed by the redistribution of trapped carriers, either as a change in the *junction capacitance* (which occurs because the depletion region will contract as negative charge is lost and the positive charge density increases) or by monitoring the *current* which results from the motion of this charge. However, the observation of capacitance transients

FIG. 5. Schematic of four different types of sub-bandgap optical transitions. Optical tran-sitions are shown by the wavy lines, and thermal transitions are shown by the vertical solid arrows. Horizontal arrows indicate the subsequent motion of the released carriers.
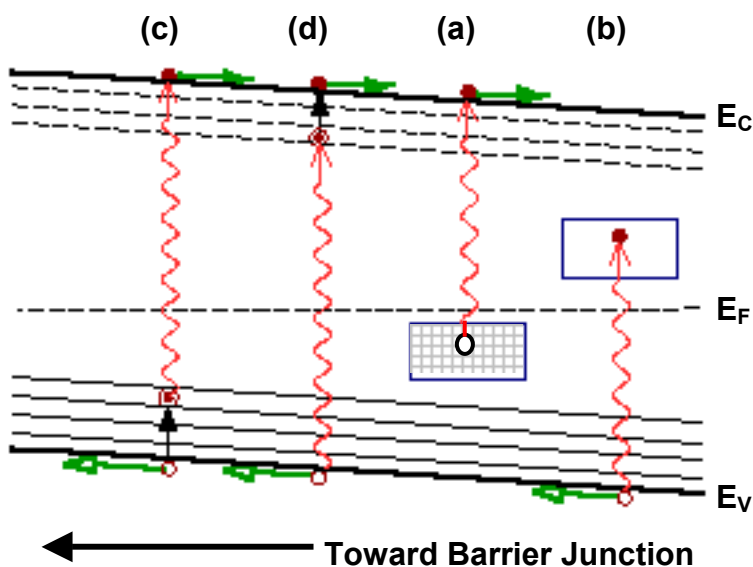
has one significant difference compared to current transient measurements: The dominant type of emitted carrier (electron or hole) can be identified by the *sign* of the observed change in capacitance.

Figure 5 distinguishes four types of optical transitions involving gap states.[16] Type (a) is the removal of an electron from an occupied defect level into the conduction band with the subsequent escape of the electron. Type (b) represents the optical excitation between the valence band and an unoccupied defect states with the subsequent escape of the valence band hole. Such a transition results in a photocapacitance signal of negative sign. Generally, such negative photocapacitance signals occur only in very intrinsic material and are even fairly rare in those cases. However, they have been recently been observed in some HWCVD a-Si,Ge:H samples discussed in Section 5, and in some of the nc-Si:H mixed phase material discussed in Section 4.

Transitions of type (c) are similar to type (a) except that, because the hole left in the gap state lies close to the valence band, it will be quickly thermally emitted into the valence band where it then also escapes the depletion region. Such a case results in no change in charge state within the depletion and, hence, no photocapacitance signal. Similarly, [Type (d)] for a transition from the valence band into an unoccupied gap state close to the conduction band, the electron will be quickly thermally emitted into the conduction band and leave the depletion region as well, with nearly zero photocapacitance signal. Ttransitions of types (c) and (d) will be dominant when the photon energy lies only slightly below the bandgap energy. In those cases, then, each photon effectively produces one valence band hole plus one conduction band electron with no net change in the gap state occupation. However, the photocapacitance signal in this energy regime does not vanish; rather, it is substantially *positive*. This thus indicates that photogenerated electrons are more likely to escape the depletion region than photogenerated holes. Moreover, while transitions of types (c) and (d) result in small changes in the junction capacitance, they result in a large junction photocurrent.

We can use such comparisons to estimate the relative collection fractions for minority vs. majority cases. If our sub-bandgap light results in n_e electrons and n_h holes leaving the depletion within the experimental time window, then the junction photocurrent signal will be proportional to $n_e + n_h$, while the photocapacitance signal will be proportional to $n_e - n_h$. Thus, it is really only by measurements of *both* the transient photocapacitance (TPC) signal *as well as* the transient photocurrent (TPI) signal that we can truly distinguish the quantities of holes and electrons excited out of the depletion region due to the sub-bandgap light. This ability to distinguish electron from hole processes is unique among all the various types of sub-band-gap optical spectroscopies.

4.0   PROPERTIES OF UNITED SOLAR NANOCRYSTALLINE SILICON

We began an effort to understand nanocrystalline silicon materials several years ago, and some of our most successful results have been obtained on sample devices obtained from United Solar Ovonic Corporation. Our first results on these materials were published in early 2006 [17] under funding by our previous NREL Subcontract. Those samples were not actual solar cells, but instead a special sandwich structure incorporating two a-Si:H cladding layers to prevent oxygen diffusion into the nc-Si:H layer. In 2006 we presented results on a newer series of nc-Si:H samples that were actual n-i-p working devices. These results appeared recently in the Conference Proceedings of the Materials Research Society.[Publ. 1] For that study we focused on samples with smaller crystalline fractions since those seemed to exhibit the best performance. During the past year we have been examining an fairly extensive series of new sample devices that were deposition using different hydrogen profiling functions, and also which encompassed a wider range of crystalline fractions (see Section 2.1 above)

4.1 DRIVE-LEVEL CAPACITANCE PROFILES vs. HYDROGEN PROFILES

In Fig. 6 we display the DLC profiles obtained for the deposition with constant hydrogen dilution at two locations corresponding to very different crystalline fractions (15125-74 and 15125-94). Results both in the annealed state (State A) and a light degraded state (State B) are shown. The light-soaked state was produced by exposing each sample to 610nm bandpass filtered light from a tungsten-halogen light source at 200mW/cm^2 intensity for 100 hours. The 785nm Raman spectra are shown again for reference. The response in these drive-level profiles do not provide significant evidence that the functionally graded H$_2$ dilutions directly affected the variation of the defect densities over the film thickness. Rather, the deep defect response, which is manifested as an increase in DLCP density with temperature, was found to be highly dependent on the crystalline volume fractions in the neighborhood of the ITO contact where each profile was taken. Specifically, a significant deep defect response after light-soaking was *only* observed in the drive-level profiles for the most crystalline materials. Also, in agreement with our previously reported results, that light-soaking actually slightly decreased the deep defect response for the more amorphous sample. This, we believe, is due to a downward shift of the relative electrical potential of the amorphous phase relative to the nano-crystallite phase. [18] In contrast, however, the deep defect response for the more crystalline sample is substantially increased after light-soaking.

In Fig. 7 we display the DLCP profiles in the light degraded states for a third sample from this deposition (15125-75) whose Raman spectrum indicated an degree of crystallinity intermediate between between those of Fig. 6. Here we observe a variation in the electronic
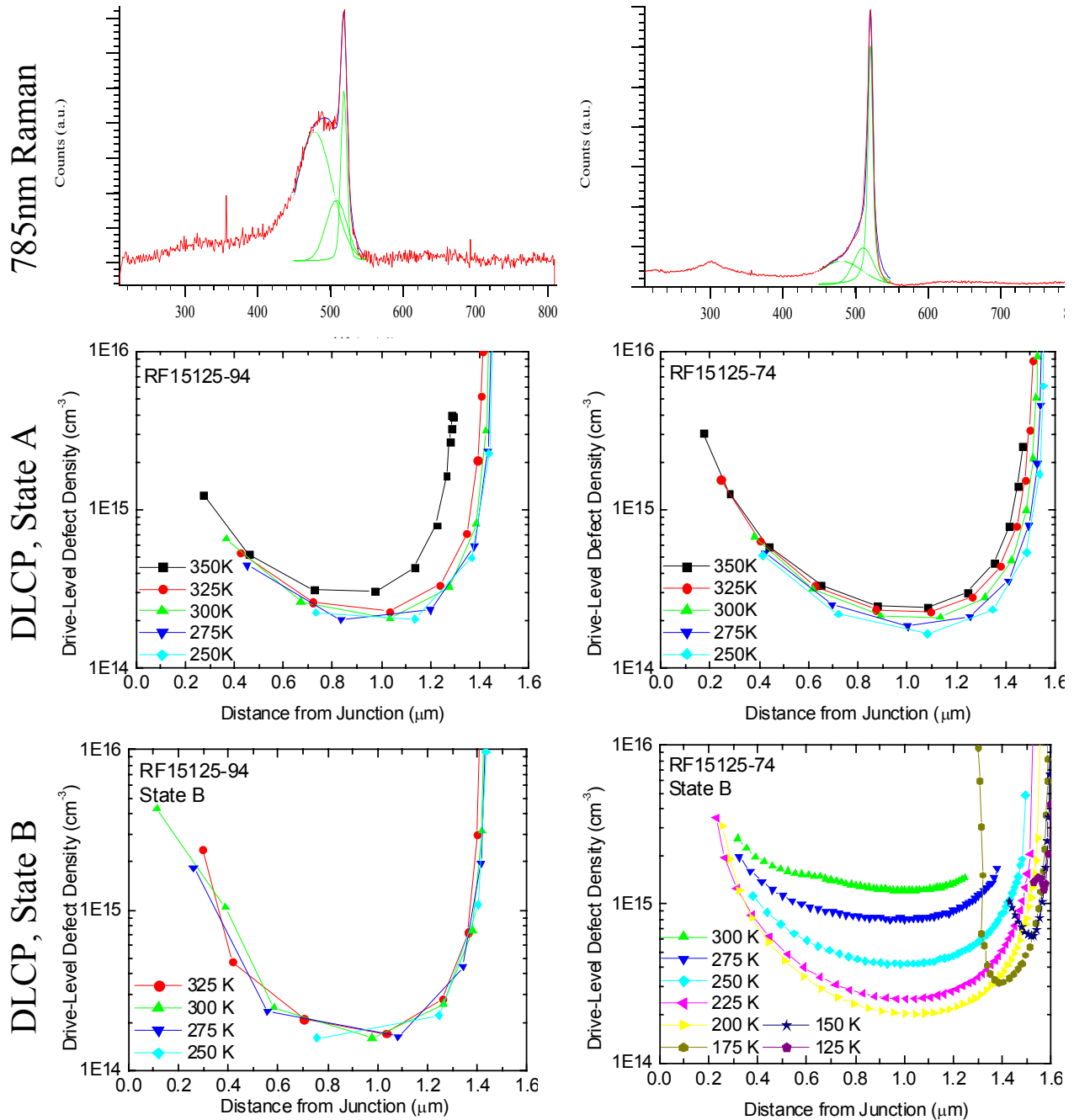
FIG. 6. Raman spectra and drive-level profiles for the least and most crystalline nc-Si:H samples from deposition 15125, before and after light-soaking. Consistent with our previous results on lower crystalline fraction samples [18], light-soaking actually appears to decrease the DLCP defect density for sample 15125-94. However, for the higher crystalline fraction sample 15125-74, light-soaking significantly increases the deep defect response.

properties after light-soaking, presumably reflecting a region with higher crystalline fraction near the top region of this sample. This corresponds to later in the deposition and, indeed, using

FIG. 7. Raman spectrum and State B drive-level profiles for deposition 15125 in a region with a crystalline fraction that is intermediate betw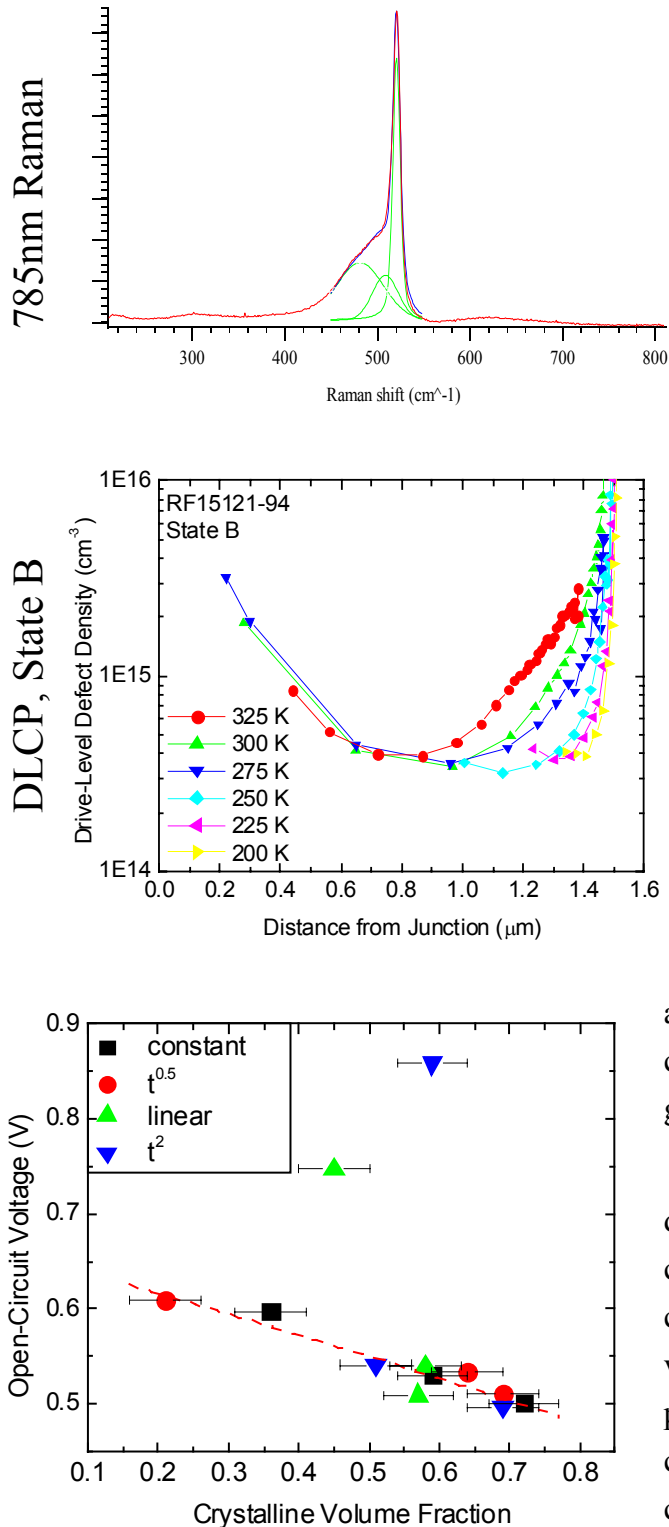een those displayed in Fig. 6. Note that the light-induced degradation in this case results in an increase in the deep defect response in only one spatial region of the sample, and this likely corresponds to the region with the higher crystalline fraction.

FIG 8. The open-circuit voltage generally increases with decreasing crystalline fraction. However, the most disordered cells grown under linear and t^2 H_2 dilution deviated significantly from this trend.

a constant hydrogen dilution we expect the crystalline fraction to increase during film growth.

Even though the DLCP densities we determined were well correlated with the crystalline volume fractions, strong correlations were *not* seen between crystal volume fraction and the cell performance parameters such as FF. However, when a comparison was made between the open-circuit voltage and crystalline fraction (Fig. 2) a general trend of a monotonic decrease in V_{oc} with increasing crystalline fraction was observed. Strong deviations in this trend occurred only in the cases of the most
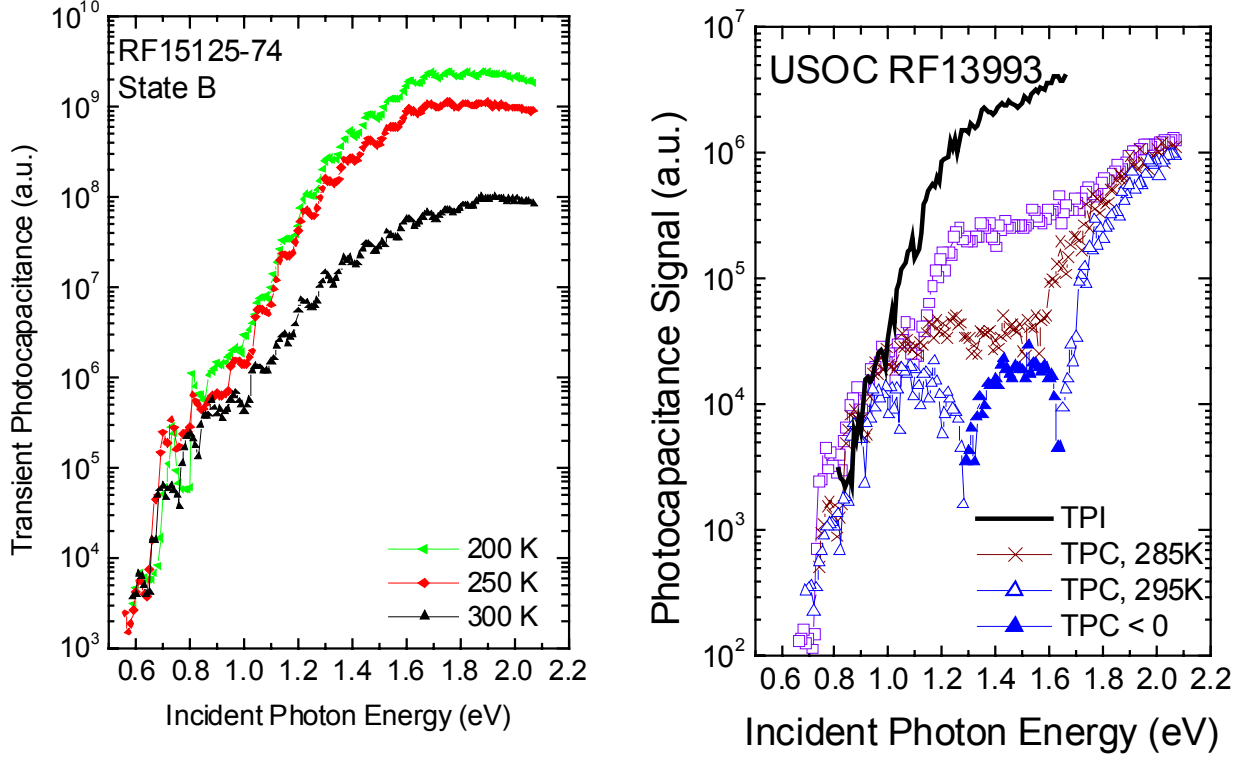
FIG 9. Transient photocapacitance (TPC) and transient photocurrent (TPI) spectra for a device with X_c=0.72±0.5 (Fig. 9a) and a previously measured device with X_c=0.53±0.5 (Fig. 9b) at different temperatures showing notably different degrees of minority carrier collection.

disordered cells grown under the most strongly varying H_2 dilution conditions. We believe it likely that such deviations arise from a concentration of disorder in these cells in a relatively small volume of the intrinsic layer in the neighborhood of the *p+/i* junction.

4.2 SUB-BAND-GAP PHOTOCAPACITANCE AND PHOTOCURRENT SPECTROSCOPY

In order to obtain a more complete picture of the energy distribution of the defects, we also began to compile TPC and TPI spectra for a subset of these samples. As previously reported [17,Publ. 1] these defects appear in the sub-bandgap absorption spectra at energies of roughly half the *a*-Si:H bandgap (Fig. 9). In addition, these spectra indicated a strong temperature-dependence in the minority carrier collection, as determined from the ratio: TPC/TPI $\propto$ (*n - p*)/(*n + p*). Generally, it has been observed that the devices having a stronger crystalline TPC nature (that is, those exhibiting a response characterized by an apparent band edge of ~1.2eV, such as in Fig 9a) also exhibit lower relative fractions of minority carrier collection above the crystalline Si bandgap energy. On the other hand, those materials exhibiting TPC spectra with a visible *a*-Si:H bandtail below 1.8eV (Fig. 9b) seemed to exhibit much larger relative minority carrier collection fractions.

5.0 NREL HOT-WIRE AMORPHOUS SILICON-GERMANIUM ALLOYS

5.1 REVIEW OF PREVIOUS WORK

A couple years ago we reported that a-Si,Ge:H alloys grown by the hot-wire chemical vapor deposition (HWCVD) method could exhibit electronic properties as good as the best glow discharge (PECVD) a-Si,Ge:H alloy films.[19,20] This resulted from replacing the usual tungsten filament with tantalum and using a filament temperature of ~1800°C instead of ~2000°C. In late Spring 2005, however, a new series of such a-Si,Ge:H films were found to have substantially inferior properties (higher defect densities and broader bandtail distributions). Subsequent SIMS analysis determined that these more recent samples contained significantly higher oxygen levels due to a contaminated GeH_4 gas line. This apparent sensitivity to oxygen impurities was, however, very surprising because similar levels of oxygen have not been found to appreciably affect the properties of a-Si:H. [21]

The source of oxygen contamination during the HWCVD growth process was identified and eliminated in the Fall, 2005. We then decided to investigate the effect of a controlled change in the level of oxygen contamination to directly find out how it was affecting the electronic properties of these samples. Therefore, series of a-Si,Ge:H alloy samples were deposited using a controlled leak valve to introduce a systematic variation in oxygen level during the HWCVD process. Oxygen levels varied from less than 1×10^{19} cm^{-3}, with no intentional air leak, to about 5×10^{20} cm^{-3}, when the air-leak was at 0.2 sccm (see Fig. 3 in Section 2). All of these a-Si,Ge:H films were deposited simultaneously on stainless steel and p^+ c-Si substrates. More of the details of these samples are described in Section 2.2.

In Fig. 10 we plot the observed spatial profile of deep defect densities as measured by DLCP technique for the four a-Si,Ge:H alloy samples with 30at.% Ge. We see that the deep defect density in the annealed State A increases from a value $\sim 8 \times 10^{15}/cm^3$ in sample A (lowest oxygen) to $\sim 2 \times 10^{16}/cm^3$ in sample D (highest oxygen). These samples were also examined in a degraded State B produced by light soaking for 100 hours at roughly $1W/cm^2$ intensity using a ELH source with a 610nm long pass filter. The deep defect densities of the samples with different oxygen contents, did increase somewhat, although less than a factor of 2 in all cases.

In Fig. 11 we display the TPC spectra in State A of the same series of 30at.% Ge sample grown with no intentional air-leak, the one with the 0.06 sccm air flow, and the one with the 0.2 sccm air flow, all on stainless steel substrates. It appears that the increased oxygen content actually results in films with narrower bandtails. While this was our initial conclusion, further study has indicated that it was not correct. Instead, we have now determined that the oxygen contamination is responsible for an additional transition between the valence band and an deep
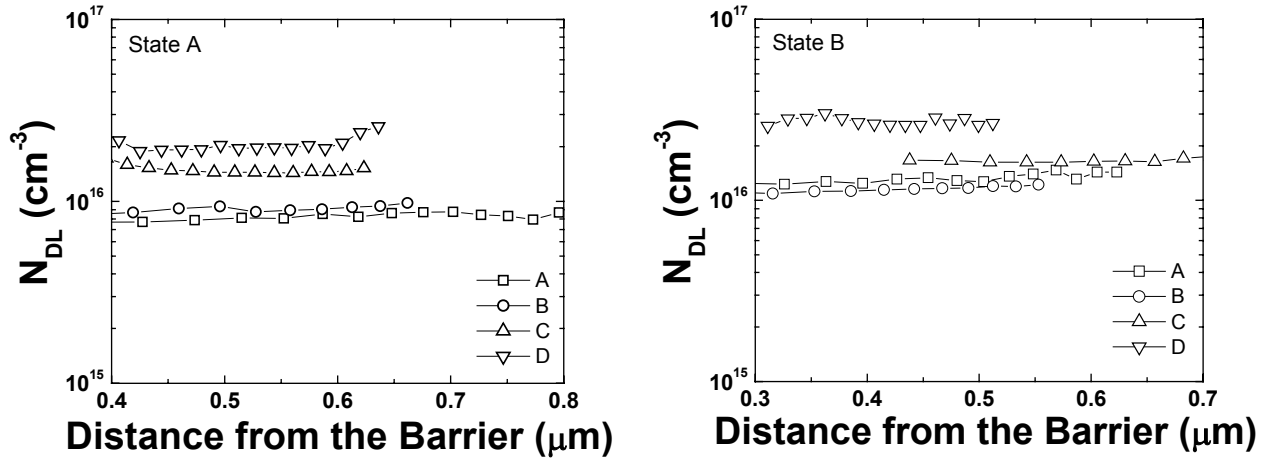
FIG. 10. Spatial profiles of HWCVD a-Si$_{0.70}$Ge$_{0.30}$:H deep defect densities with different oxygen levels in (a) the annealed State A and (b) in a light-soaked State B. These DLC profiles were obtained at 1.1 kHz and 370K.

defect level. This results in a negative TPC signal that overlaps the bandtail region thus making it appear to be more narrow. The details of what we have been able to learn about this oxygen related defect became a primary focus of our work on the HWCVD a-Si,Ge:H alloys carried out this past year.

FIG 11. TPC spectra for 3 of the HWCVD a-Si$_{0.70}$Ge$_{0.30}$:H films with different oxygen levels deposited onto p$^+$ c-Si substrates. These curves have been vertically offset for display purposes. The Urbach energies for samples A, C, and D appear to be 43, 38, and 45 meV, respectively. However, this is not correct; instead, this apparent narrowing of the bandtail is actually due to the presence of a second defect transition that produces a negative TPC signal centered roughly between 1.3eV to 1.4eV.
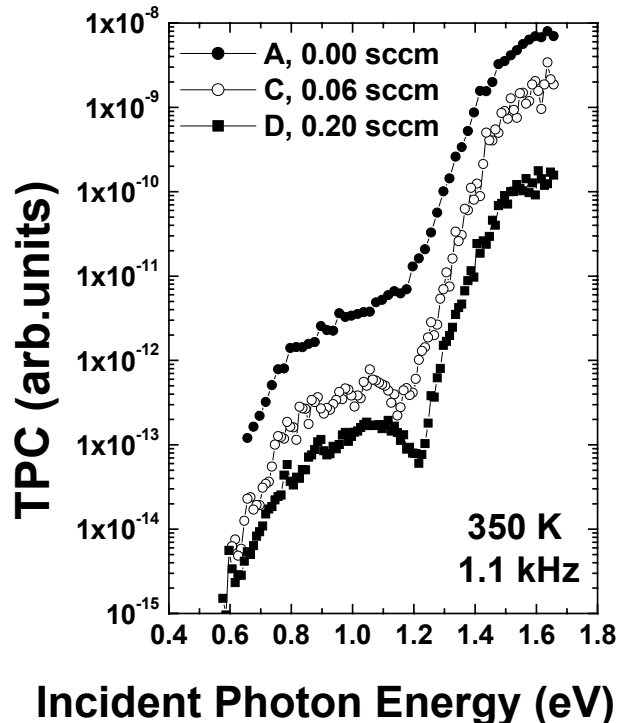
5.2 AN OXYGEN RELATED DEFECT IN HWCVD a-Si,Ge:H

In Fig. 12 we display the TPC spectra for the 0 and 0.06 sccm leak rate samples along with transient photocurrent (TPI) spectra taken under the same temperature and rate window. As previously discussed, the TPC spectra correspond to the *difference* of electron and hole carriers collected at each photon energy, while the TPI spectra correspond to the *sum* of these. Thus, by examining both types of spectra together one can deduce the fractions of each. The thin solid lines appearing along with these spectra indicate detailed fits that we have carried out to reproduce their salient features.

For the sample deposited without an intentional air leak the spectra indicate two specific features: electronic excitation from a gaussian shaped defect band to the conduction band with an optical energy threshold of 0.82eV (FWHM of 0.17eV), plus a exponential bandtail with an Urbach energy of 45 meV. The ratio of the TPI to TPC signals in the bandtail region indicates the relative collection fractions of holes to electrons to holes. It is 99% for this sample, among the highest ever deduced by this method.

The TPC spectra for the sample with the 0.06sccm air leak appears to exhibit an even narrower bandtail; however, when taken together with the TPI spectrum in Fig. 13 we have now discovered this is *not* the case. Instead, to obtain a good fit to both types of spectra together we must include the effects of an additional defect band that has an optical threshold centered at 1.4eV *from the valence band*. Taken together with an Urbach energy of 47meV as well as a defect band centered 0.85eV below the conduction band, a good fit is obtained to both the TPC and TPI spectra as indicated. In this case the relative collection fraction of holes/electrons is found to be 95%. This is quite consistent with the 47meV value of Urbach energy that we have deduced in our detailed fitting of these spectra.

A light-soaked state of both samples was examined after exposure to 610nm filtered light from an ELH source for 100hours at an intensity of 400mW/cm^2. The role of the additional defect band is even more apparent in the spectra of the light soaked state of the 0.06sccm air-leak sample that is displayed in Fig. 12(b). Here we find that it has a similar or perhaps even a slightly smaller magnitude than for State A. The defect band at $E_C - 0.85$eV, on the other hand, was found to increase, but only by a factor of about 1.5. The same factor increase was found for DLCP data obtained before and after light-soaking this sample. (The Urbach energy used to obtain the fits to the spectra in the light-soaked state was again 47meV.) Somewhat surprisingly the hole/electron collection fraction appears to have *increased* (to above 98%).
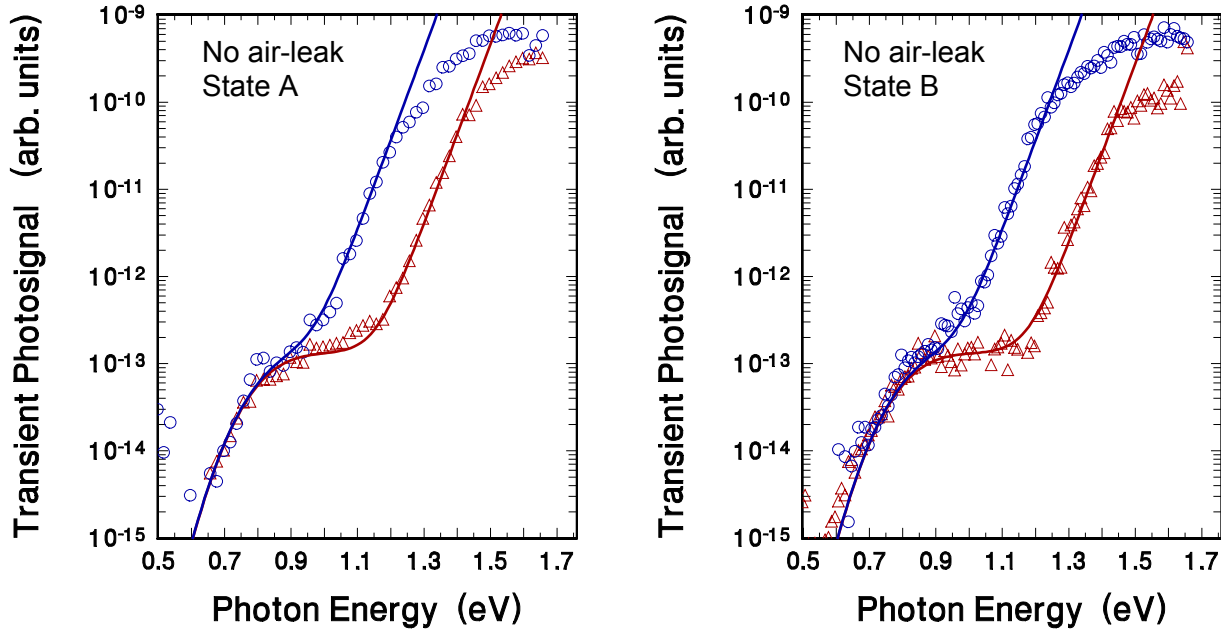
FIG. 12. TPC and TPI spectra before and after light-soaking for the a-Si$_{0.70}$Ge$_{0.30}$:H film deposited without an intentional air leak. The solid lines represent a fit to these spectra indicating a defect band 0.82 Ev below E$_C$ with a FWHM of 0.17eV, plus an Urbach energy of 45meV.
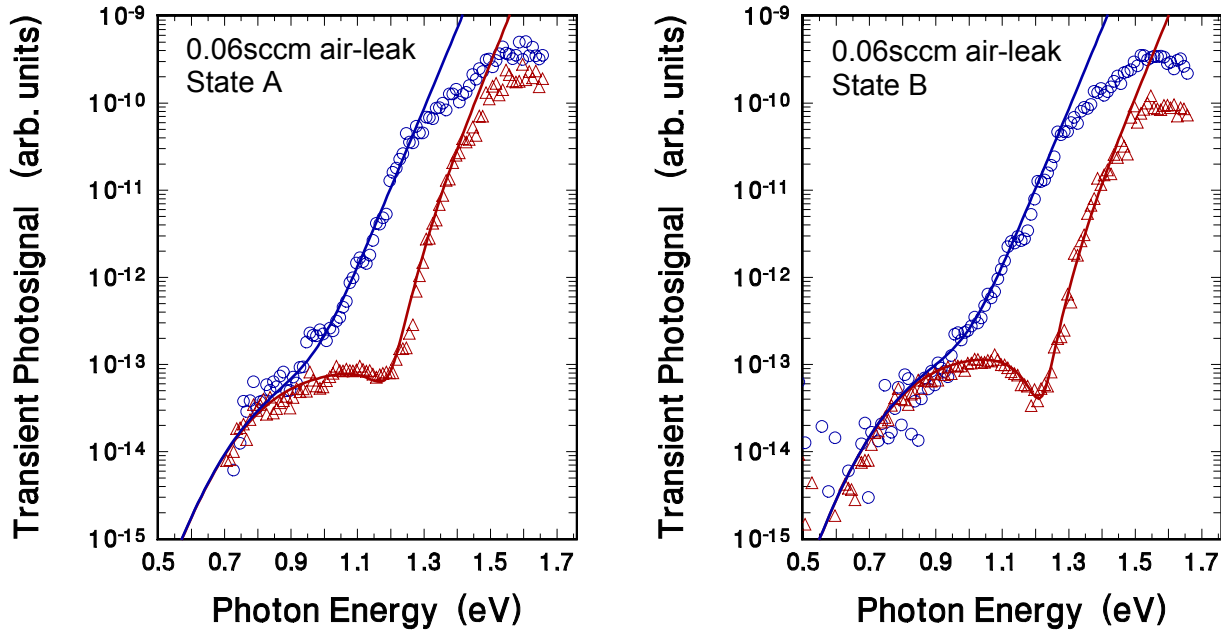
FIG. 13. TPC and TPI spectra before and after light-soaking for the a-Si$_{0.70}$Ge$_{0.30}$:H film deposited with the 0.06sccm air leak. The fits in this case indicate a defect band 0.85eV below E$_C$ (FWHM = 0.24eV) *plus a second band of defect transitions* at 1.4 eV above E$_V$.(also with FWHM = 0.24eV). The deduced Urbach energy required to fit *both* the TPC and TPI spectra is now 47meV.

For the sample without intentional oxygen contamination we also observed an increase in the hole/electron collection fraction (to 99.4%). We found nearly *no change* in the magnitude of

the $E_C - 0.82eV$ defect band. The DLCP data also indicated very little change in the midgap defect density after light-soaking for this sample (see Fig. 10).

Figure 14 exhibits a comparison of the TPC spectra for three samples with increasing oxygen levels. We see that the 1.4eV transition is basically absent from the spectrum of the sample with no intentional oxygen incorporation during the HWCVD growth, and increases with as the oxygen level increases. We thus attribute this 2nd defect band with the oxygen impurities present in these a-Si$_{0.7}$Ge$_{0.3}$:H alloy films. However, this increased oxygen level appears to have only a very minor effect upon the minority carrier collection fraction. For the lowest oxygen sample we deduce an Urbach energy of 45meV, among the lowest ever measured for a a-Si,Ge:H sample in this alloy range. Correspondingly, the relative collection fraction of hole-to electron was found to be around 97% for that sample. Moreover, as indicated in Figs. 12 and 13, these HWCVD deposited a-Si,Ge:H films appear to be much more stable with respect to light-induced degradation than the highest quality PECVD a-Si,Ge:H samples studied [22] previously by these methods. However, this may partially be because their initial deep defect densities are close to 10^{16} cm^{-3}, compared to the mid 10^{15} cm^{-3} level of those previous PECVD samples.
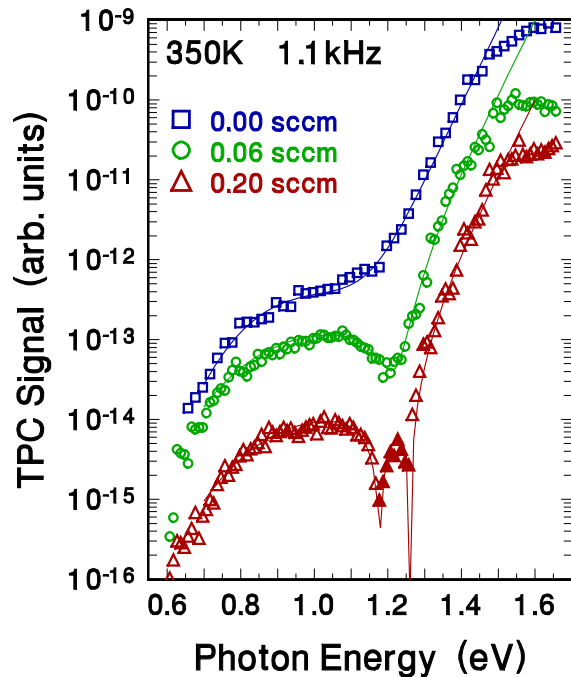
FIG. 14. Photocapacitance spectra for three a-Si$_{0.7}$Ge$_{0.3}$:H samples with different oxygen levels. The thin solid lines indicate fits obtained in the same manner as those in Figs. 12 and 13. For the sample with highest oxygen content, the TPC signal actually became *negative* (filled triangles) for the region between 1.1 and 1.4eV.

FIG. 15. TPC spectra of the highest oxygen a-Si$_{0.7}$Ge$_{0.3}$:H sample at 3 temperatures. These spectra were been vertically shifted from each other for greater visibility. Note the relative increase of the negative feature (filled symbols) near 1.2eV at higher temperatures, and the relative decrease in the bandtail signal.

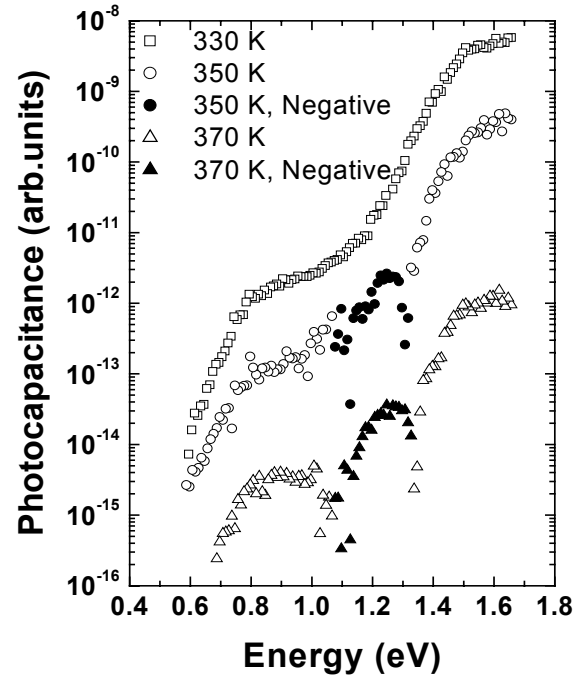**FIG. 16.** Temperature variation of the TPC signal at photon energies near 1.2 eV. These data clearly indicate that the negative TPC signal from the oxygen related defect is largest at 375K, then falls off at higher temperatures due to the increase emission rate of its electron to the conduction band. The rapid increase to positive values at temperatures below 350K is partially due to the increasing contribution from the bandtail signal, which becomes larger as the relative fraction of minority carrier collection decreases.
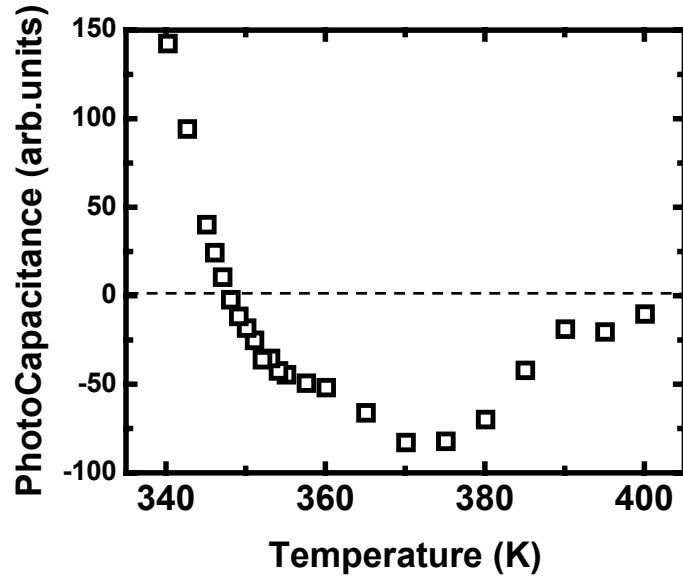
One interesting remaining issue concerns why the transition into an empty defect band at ~1.4eV from the valence band should be so predominantly negative for the sample with the highest oxygen level. This can only be possible if the electron that is inserted from the valence band remains strongly trapped for the duration of the measurement time window (of roughly 0.4s). We attempted to study the subsequent thermal emission of this trapped electron by recording the TPC spectra for the highest oxygen doped sample over a wider range of temperatures. Three such spectra are shown in Fig. 15. In Fig. 16, we plot the temperature dependence of the TPC signal at a photon energy of 1.2eV (where the signal due to the 1.4eV transition is clearly visible and is also less obscured by the bandtail signal). This temperature dependence indicates that the (negative) contribution due to the oxygen impurity peaks near 375K. Moreover, above ~380K, the photocapacitance signal is reduced in magnitude due to the subsequent thermal emission of this optically trapped electron from this 2nd defect state. Also, below about 345K the TPC signal increases monotonically to a large positive value. We believe this is due to an increasing positive contribution from the bandtail which is always found to become significantly larger at lower temperatures (as is also evident in Fig. 15).

Based on these experimental results, we hypothesize that the observed oxygen impurity related defect state is associated with a positively charged oxygen donor level, possibly that previously suggested three fold coordinated (O_3^+) type centers in a-Si:H [23- 24, 25,26]. The 1.4eV transition energy from the valence band indicates a center close to the conduction band; however, to account for the observed behavior, it is also necessary that in the O_3^0 state, the trapped electron cannot be thermally emitted into the conduction band very quickly. This clearly requires the presence of a significant thermal barrier to inhibit this.

6.0 COPPER INDIUM-GALLIUM DISELENIDE SOLAR CELLS:
THE ROLE OF SODIUM

For the CIGS portion of work supported this Subcontract we have been applying our measurement techniques to try to understand differences between the best laboratory cells, and those fabricated using processes better suited for manufacturing. For this Subcontract year we are reporting what we have learned about the role of Na in improving the performance of CIGS based devices.

The addition of Na to the CIGS absorber layer is a commonly followed procedure, boosting the efficiency by up to 50% primarily through a sizeable increase in the open-circuit voltage (V_{oc}) and the fill factor (FF). Although the positive role of Na is well known, there is an ongoing debate as to the exact mechanism of the beneficial effect of Na, with much of the debate centering around where in the cell the Na has its effect. Possible sites are grain boundaries, in the bulk of the grains, or the CdS/CIGS heterojunction. Recent experimental results appear quite contradictory, with one group finding no evidence of Na at the grain boundaries[27] and another group concluding that the Na is only found in significant amounts at the grain boundaries[28]. Another group hypothesizes that the Na acts only during the growth of the sample to organize and passivate point defects[29]; however, this is disputed by similar benefits obtained through diffusion of Na into the sample in a post-deposition treatment[30].

As described in Section 2.3, a pair of matched baseline and reduced Na samples were provided to us by the Institute of Energy Conversion in May, 2006. The baseline film was deposited on a Mo-coated soda lime glass substrate and the reduced Na film was deposited on a substrate that had a SiO_2 diffusion barrier below the Mo.   The presence of Na resulted in the
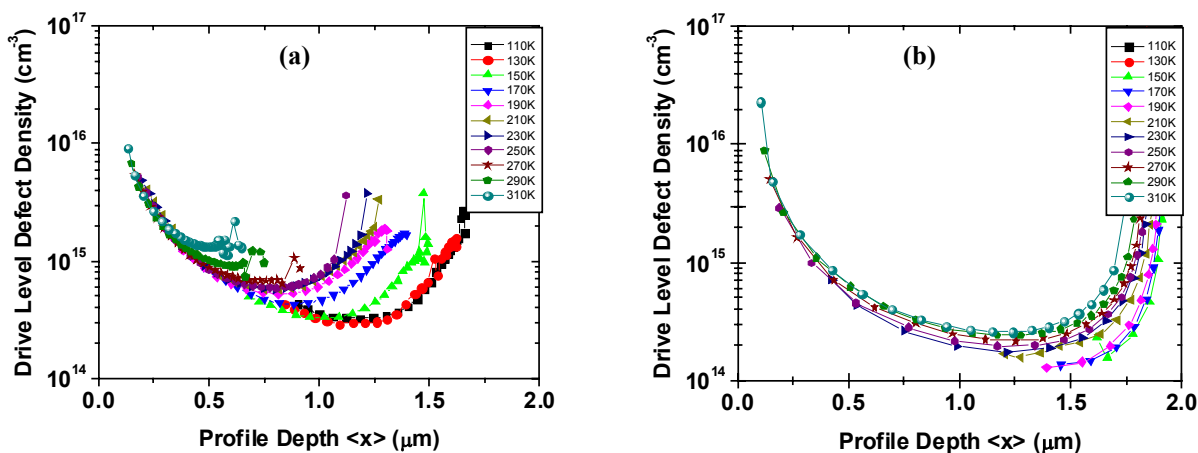

FIG. 17. DLC Profiles for (a) Na and (b) reduced Na CIGS samples. These profiles were obtained at 10 kHz at the temperatures indicated with an applied dc biases from 1.0 V reverse to 0.3 V forward. The profiles have similar shapes, and the higher Na sample appears to exhibit a larger deep defect response. However, that cell is 50% more efficient than the reduced Na cell.

well known beneficial effects on the solar cells: An increased V_{oc}, fill factor, and efficiency (by more than 40%), with virtually no effect on short circuit current (see Table IV in Section 2.3).

Drive-level capacitance profiles are displayed for the CIGS samples with and without Na in Fig. 17. These profiles show similar overall shapes but more spatial variation in the sample with Na. The sample with Na shows a defect activating between 130 K and 190 K that is absent in the reduced Na sample. Without any prior knowledge of cell performance, one would predict that the more spatially uniform, reduced Na sample to be more efficient. Exactly the opposite is the case. Thus, this indicates that something not visible in the DLC profiles is having a dramatically harmful effect on the performance of the low Na cell.

These profiles indicate free carrier densities of 3×10^{14} cm^{-3} for the Na sample and 1.2×10^{14} cm^{-3} for the reduced Na sample. From the higher temperature profiles we infer a deep acceptor density of $\sim 1 \times 10^{15}$ cm^{-3} in the higher Na sample. The reduced Na sample does not show this type of defect, instead it increases only slightly with temperature to a maximum value of $\sim 3 \times 10^{14}$ cm^{-3}. The abrupt increase in the DLC profiles near the junction ($<x> = 0$) may reflect a significant defect density near the junction, however we are not certain whether the DLCP can provide an accurate measurement of the defect density in this region. We thus choose to use the more spatially uniform region of the profiles to estimate the free carrier and defect densities.

In Fig. 18 we compare the TPC spectra for the Na and reduced Na samples. The spectra have been aligned above the 1.2 eV gap energy to enable a better comparison. The spectra are surprisingly similar, and the thin solid lines indicate fits in which we have assumed a gaussian defect band and an exponential band tail. The sample containing Na exhibits an Urbach energy of 17 meV plus a gaussian defect band centered at 0.75 eV above E_V with a FWHM near 120 meV. The Urbach energy for the low Na sample is larger, 23 meV, and the gaussian defect band appears centered at 0.70 eV with a much smaller width, about 50 meV. The narrower bandtail for the sample with Na suggests a higher degree of crystalline order within the CIGS absorber[31].
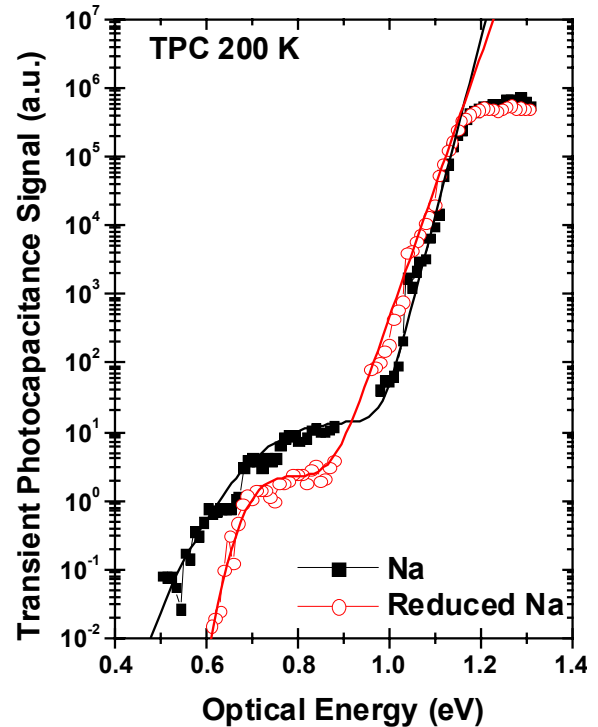

FIG. 18. TPC Spectra of the two CIGS samples with normal and reduced Na. The reduced Na sample spectrum exhibits a broader bandtail, indicating a higher level of disorder.

Admittance spectra were obtained for each of these samples for frequencies between 100 Hz and 100 kHz and temperatures between 80 K and 280 K. With 0 V applied bias, there is a very distinct activated step in the sample with Na, but no such clear feature in the reduced Na sample, as shown in Fig. 19(a) and (b). The step in the Na sample has an activation energy of 270 meV as determined by an Arrhenius plot, consistent with many previous admittance measurements of CIGS materials. It is worth pointing out that many researchers have associated such a larger step in admittance with poorer device performance. However, in this case, the exact opposite appears to be true.

Admittance spectra were then obtained over the same frequency ranges, but with an applied bias. Under reverse bias of 0.5 V, there were no changes in the spectra. The reduced Na sample spectra looked the same, and the magnitude of the step in the Na sample spectra changed in the manner expected for a bulk defect. The surprise came when the admittance spectra were obtained under forward bias. The reduced Na sample showed a clear activated step, while the higher Na sample showed only a hint of an additional step, as shown in Fig. 19(c) and (d).

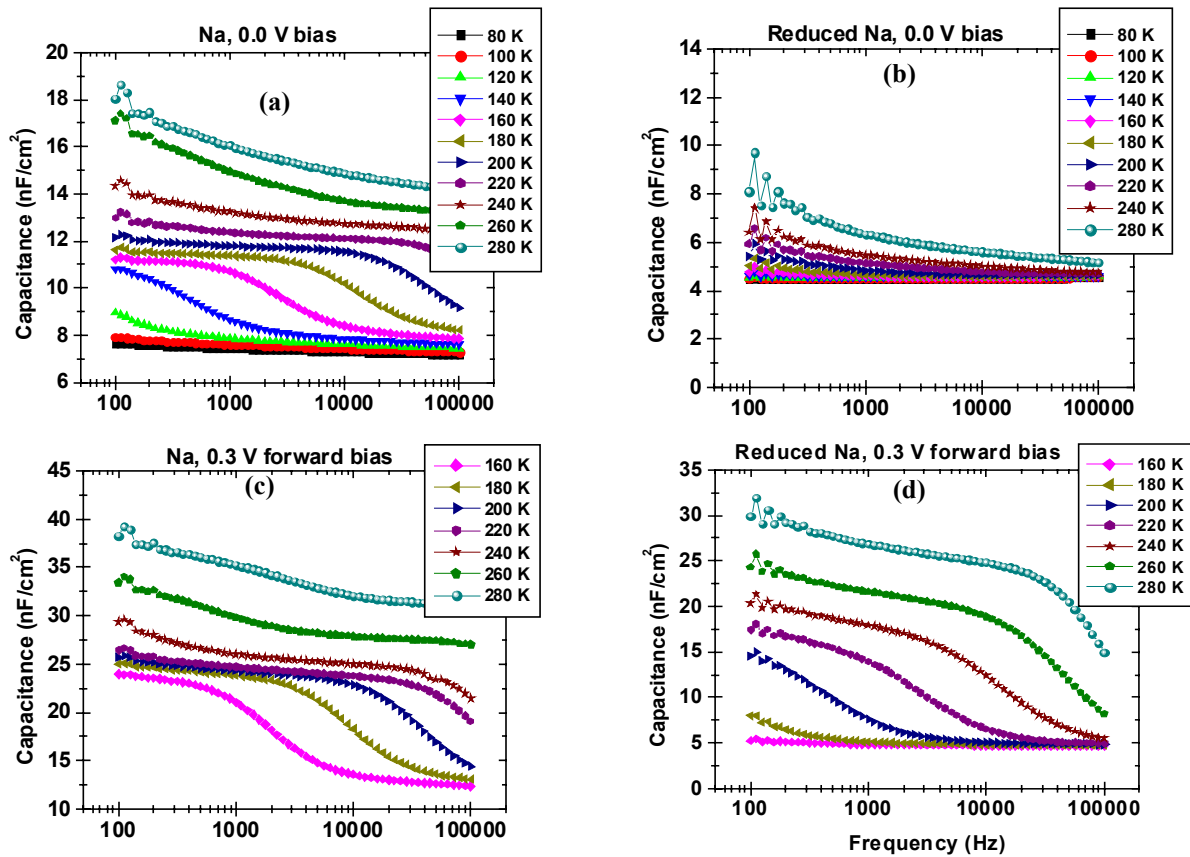For the admittance data shown in Fig. 20, we varied the forward bias while keeping the

FIG. 19. Admittance spectra for (a) & (c) the Na containing sample, and (b) & (d) the reduced Na sample. The reduced Na sample shows a step only visible under an applied forward bias.
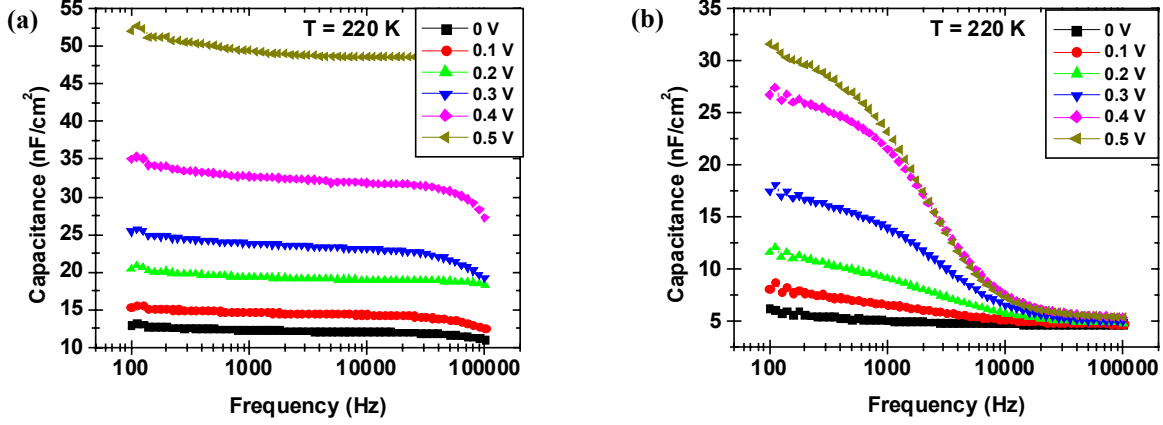
FIG. 20. Admittance vs applied voltage for (a) Na sample, 280 K and (b) reduced Na sample, 220 K. The appearance of the capacitive step under forward bias and the limit in its magnitude for the reduced Na sample are both characteristic responses of an significant interface state.

temperature constant. Here one sees the further development of this effect. In this case the reduced Na sample shows a very clear step between 180 K and 300 K, with an activation energy of 380 meV. The type of behavior exhibited in this figure clearly indicates the presence of large density of states near the interface for the reduced Na sample compared to the sample with higher Na. Specifically, the capacitance of the Na sample increases without any apparent bound as the forward bias is increased whereas, for the reduced Na sample, one appears to reach a limit near 35 nF/cm^2. This limit is indicative of a defect near the barrier interface that becomes more and more charged with increasing forward bias, thus limiting the collapse of the depletion region under forward bias. The fact that the step only appears under a limited range of bias also indicates that this defect is located in the interface.

The differing behavior under forward bias is by far the most profound difference between the Na and reduced Na samples, and so seems the most likely candidate to explain the difference in performance. Indeed, a sufficient large defect density in close proximity to the CdS/CIGS interface could easily affect the band bending and result in the 130mV observed difference in V_{oc}. If we assign this open circuit voltage loss exclusively to this defect, then by integrating Poisson's equation, we can estimate the amount of extra charge that is accumulating near the interface. Namely,

$$\Delta V = \frac{1}{\varepsilon} \int_0^\infty x\rho(x)dx \approx \frac{qN_{int}d}{\varepsilon} , \qquad (3)$$

where qN_{int} is the total sheet charge density present near the open circuit voltage condition, and d is the width of its spatial distribution from the barrier interface. For example, if we assume that d is 50 nm, then a 0.13 V difference in the device voltage requires a change of sheet charge density 1.6×10^{11} cm^{-2}.

We have also tried to reconcile this estimate with the results of our admittance and DLCP measurements discussed above. Figure 6 shows numerical calculations in which we place a deep defect of areal density near 10^{12} cm^{-2} within roughly 0.2 μm of the barrier interface, broadly distributed in energy. The change in its occupation over a change in bias equal to V_{OC} is then quite close to the above estimate. We see that it is then possible to closely reproduce both the observed drive-level profiles under forward bias exhibited by the reduced Na sample. We are currently pursuing further numerical modeling to attempt to also account in detail for both the admittance and cell performance behavior with such an assumed distribution of defect states near the barrier interface.
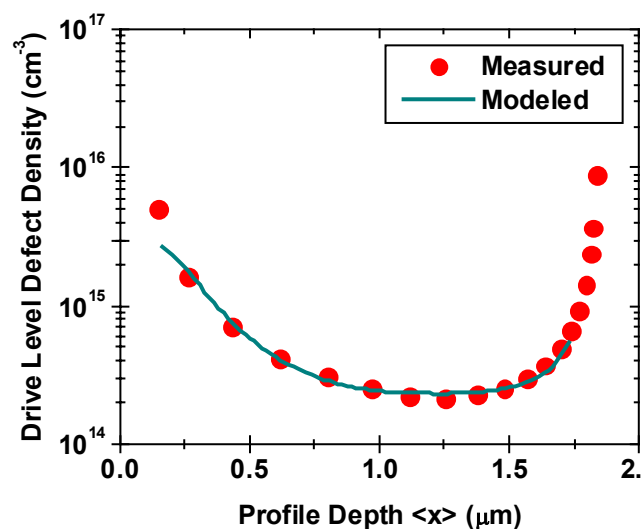
FIG. 21. Comparison of the experimental reduced-Na CIGS DLC profile (solid circles) with a calculation (line) based upon an assumed distribution of defects near the barrier interface.

7.0 SUMMARY AND PLANS FOR FOLLOW-UP STUDIES

During Phase II of our NREL Subcontract period we have again focused on the three areas of study pursued in Phase I. First, we have continued our work to characterize the electronic properties of nc-Si:H materials obtained from United Solar. A quite extensive set of of new sample devices were obtained, all of which were actual working n-i-p solar cell devices. These were all deposited on specular stainless-steel under four different types of hydrogen profiling, and each deposition contained samples with varying degrees of crystalline fractions.

Our data suggested that the degree of crystallinity in these nc-Si:H samples, rather than the hydrogen profiling function itself, was the strongest factor determining the defect response in our junction capacitance measurements. We also found that the samples that contained a higher fraction of amorphous component, as determined from Raman spectroscopy, exhibited the highest *resilience* to light-induced deep defect creation indicating an actual slight *decrease* in defect response as shown by DLCP measurements. This agrees with our measurements reported last year. On the other hand, the samples with estimated crystalline fractions above 60vol.% exhibited quite a pronounced increase of deep defects after light soaking.

In spite of this, all of the sample devices exhibited a decrease in performance after light soaking with 610nm filtered ELH light. Last year we reported a tentative degradation model that considered the a light-induced increase in an energetic barrier between the crystalline and amorphous components of these materials as perhaps a more important factor in limiting the device performance of such mixed phase materials than the increase in the defect density itself. This would account for the marked reduction in minority carrier collection that we have also observed in these materials [Publ. 1]. Further studies are being pursued to test this model over the wider range of nc-Si:H samples received during this past year.

Second, we have been studying in detail the set HWCVD a-Si,Ge:H alloys deposited at NREL by Yueqin Xu in which controlled levels of oxygen impurities were introduced, ranging from below $10^{19} cm^{-3}$ to roughly $5 \times 10^{20} cm^{-3}$. This past year we discovered that the oxygen was responsible for a distinct deep defect, with an optical transition lying roughly 1.3 to 1.4 eV above the valence band. We hypothesize that the observed oxygen impurity related defect state may be associated with a positively charged oxygen donor level, possibly the previously suggested three fold coordinated oxygen center (O_3^+). Moreover, because the electrons excited into this defect remain trapped for roughly 0.5s at temperatures up to 370K, this strongly implies that there must exist a large barrier to their subsequent thermal emission into the conduction band. Follow up studies will try to pin down the thermal emission energy of the electron into the conduction in order to construct a configurational coordinate diagram for the transitions involving this defect. Also, we will examine samples containing a wider range of Ge alloy fractions to ascertain whether Ge itself may be playing a central role in the appearance of this defect.

Finally, we used our junction capacitance methods to study the effect of Na on CIGS thin film solar cells. Our DLCP measurements revealed an increased free carrier density with the addition of Na and an activated bulk defect in CIGS absorber. However, neither could account for the >40% increase in efficiency with the addition of Na. The sub-band-gap TPC spectra showed a broader defect band and a steeper Urbach energy with the addition of Na which implies an increase in the carrier mobilities, but this again was not expected to lead to differences in performance consistent with the observations. Ultimately, forward bias admittance measurements revealed the existence of a large defect density at the CdS/CIGS heterojunction for the lower Na sample. It is interesting to note that SIMS profiles showed the Na moving towards the front of the cell when it is intentionally added. Finally, we argued that such a defect could readily explain the loss in V_{OC} in the sample with reduced Na, and would be consistent with the observed admittance and DLCP behavior for this sample. Thus, it appears that it is the passivation of these interfacial defects that primarily accounts for the beneficial effects of Na toward the increased performance of the CIGS solar cells fabricated at IEC.

8.0 SUBCONTRACT SUPPORTED PUBLICATIONS

1. P.G. Hugger, S. Datta, P.T. Erslev, Guozhen Yue, Gautam Ganguly, Baojie Yan, Jeffrey Yang, Subhendu Guha, and J.D. Cohen, "Electronic characterization and light-induced degradation in nc-Si:H solar cells, Mat. Res. Soc. Symp. Proc. **910**, A01-05 (2006).

2. Shouvik Datta, J. David Cohen, Steve Golledge, Yueqin Xu, A. H. Mahan, James R. Doyle and Howard M. Branz, "The effect of oxygen contamination on the electronic properties of hot-wire cvd amorphous silicon germanium alloys", Mat. Res. Soc. Symp. Proc. **910**, A02-05 (2006).

3. <u>Shouvik Datta</u>, Yueqin Xu, A. H. Mahan, Howard M. Branz, and <u>J. David Cohen</u>, "Superior structural and electronic properties for amorphous silicon-germanium alloys deposited by a low temperature hot wire chemical vapor deposition process", J. Non-Cryst. Solids **352**, 1250 (2006).

4. J. David Cohen, Shouvik Datta, Kimon Palinginis, A. H. Mahan , Eugene Iwaniczko, Yueqin Xu, and Howard M. Branz, "Defect analysis of thin film Si-based alloys deposited by hot-wire CVD using junction capacitance methods", Thin Solid Films, in press.

5. Shouvik Datta, J. David Cohen, Yueqin Xu, A.H. Mahan, and Howard M. Branz, "Dependence of the Electronic Properties of Hot-Wire CVD Amorphous Silicon-Germanium Alloys on Oxygen Impurity Levels", Mat. Res. Soc. Symp. Proc. Vol **1012** (in press).

6. Peter T. Erslev, Adam F. Halverson, J. David Cohen, and William N. Shafarman, "Study of the Electronic Properties of Matched Na-containing and Na-free CIGS Samples Using Junction Capacitance Methods", Mat. Res. Soc. Symp. Proc. Vol **1012** (in press).

9.0   REFERENCES

1.   K. Wang, D. Han, D.L. Williamson, B. Huie, J.R. Weinberg-Wolf, b. Yan, J. Yang, and S. Guha, Mater. Res. Soc. Symp. Proc. Vol. **862**, 117 (2005).

2. E. Bustarret, M.A. Hachicha, and M. Brunel, Appl. Phys. Lett. 52, 1675 (1988).

3. J.D. Cohen, NREL Report SR-520-32535 (2002).

4. C. Lei, C.M. Li, A. Rockett and I.M. Robertson, J. Appl. Phys. **101**, 024909 (2007).

5. V. Lyahovitskaya, Y. Feldman, K. Gartsman, H. Cohen, C. Cytermann, and David Cahen, J. Appl. Phys., **91**, 4205 (2002).

6. A. Rockett, *Thin Solid Films* **480-1,** 2 (2005).

7. D. Rudmann, D. Bremaud, H. Zogg and A. N. Tiwari, J. Appl. Phys. **97**, 084903 (2005).

8. D.V. Lang, J.D.Cohen, and J.P. Harbison, Phys. Rev. B**25**, 5285 (1982).

9. C.E. Michelson, A.V. Gelatos, and J.D. Cohen, Appl. Phys. Lett. **47**, 412 (1985).

10. K.K. Mahavadi, K. Zellama, J.D. Cohen, and J.P. Harbison, Phys. Rev. B**35**, 7776 (1987).

11. T. Unold, J. Hautala, and J.D. Cohen, Phys. Rev. B50, 16985 (1994).

12. J.T. Heath, J.D. Cohen, and W.N. Shafarman, J. Appl. Phys. **95**, 1000 (2004).

13. J.D. Cohen and A.V. Gelatos, in *Advances in Disordered Semiconductors Vol I: Amorphous Silicon and Related Materials*, ed. by H. Fritzsche (World Scientific, Singapore, 1988), pp. 475-512.

14. J. David Cohen, Thomas Unold, A.V. Gelatos, and C.M. Fortmann, J. Non-Cryst. Solids **141**, 142 (1992).

15. T. Unold, J.D. Cohen, and C.M. Fortmann, Mat. Res. Soc. Symp. Proc. **258**, 499 (1992).

16. A.V. Gelatos, K.K. Mahavadi, and J.D. Cohen, Appl. Phys. Lett. **53**, 403 (1988).

17. A.F. Halverson, J.J. Gutierrez, J.D. Cohen, B. Yan, J. Yang, and S. Guha, Appl. Phys. Lett. 88, 071920 (2006).

18. P.G. Hugger, S. Datta, P.T. Erslev, G. Yue, G. Ganguly, B. Yan J. Yang, S. Guha, and J.D. Cohen, Mat. Res. Soc. Symp. Proc. **910**, 21 (2006).

19. A.H. Mahan, Y. Xu, L.M. Gedvilas, R.C. Reedy, H.M. Branz, D.L. Williamson, S. Datta, J.D. Cohen, and B. Yan, Proc. 31st IEEE PV Specialists Conference-2005 (Buena Vista)

20. S. Datta, J. D. Cohen, Y.Xu, and A. H. Mahan, Mat. Res. Soc. Symp. Proc. **862**, A7.2 (2005).

21. C. E. Michelson and J.D. Cohen, Phys. Rev. B**41**, 1529 (1990).

22. Chih-Chiang Chen, Fan Zhong, J.D. Cohen, Jeffrey C. Yang, and Subhendu Guha, Phys. Rev. B**57**, R4210 (1998).

23. R. A. Street and N. F. Mott, Phys. Rev. Lett. **35**, 1293 (1975).

24. David Adler, Solar cells. **9**, 133 (1983).

25. Tatsuo Shimizu, Minoru Matsumoto, Masahiro Yoshita, Masahiko Iwami, Akiharu Morimoto, and Minoru Kumeda, J. Non-Cryst. Solids. **137&138**, 391 (1991).

26. H. Fritzsche, J. Non-Cryst. Solids. **190**, 180 (1995).

27. C. Lei, C.M. Li, A. Rockett and I.M. Robertson, J. Appl. Phys. **101**, 024909 (2007).

28. V. Lyahovitskaya, Y. Feldman, K. Gartsman, H. Cohen, C. Cytermann, and David Cahen, J. Appl. Phys., **91**, 4205 (2002).

29. A. Rockett, *Thin Solid Films* **480-1,** 2 (2005).

30. D. Rudmann, D. Bremaud, H. Zogg and A. N. Tiwari, J. Appl. Phys. **97**, 084903 (2005).

31. S.M. Wasim, C. Rincon, G. Marin, P. Bocaranda, E. Hernandez, I. Bonalde and E. Medina, Phys. Rev. B., **64**, 195101 (2001).